This is a non-peer reviewed preprint that has been submitted to *Geophys. J. Int.*

Deep Learning for Deep Earthquakes: Insights from OBS Observations of the Tonga Subduction Zone

Ziyi Xi[1,#], S. Shawn Wei[2,1,#], Weiqiang Zhu[3], Gregory C. Beroza[4], Yaqi Jie[2], Nooshin Saloor[2]

[1] *Department of Computational Mathematics, Science and Engineering, Michigan State University, East Lansing, Michigan, USA*

[2] *Department of Earth and Environmental Sciences, Michigan State University, East Lansing, Michigan, USA*

[3] *Department of Earth & Planetary Science, University of California, Berkeley, Berkeley, California, USA*

[4] *Department of Geophysics, Stanford University, Stanford, California, USA*

[#] *Correspondance to {xiziyi,swei}@msu.edu*

This is a non-peer reviewed preprint that has been submitted to Geophys. J. Int.

SUMMARY

Applications of machine learning in seismology have greatly improved our capability of detecting earthquakes in large seismic data archives. Most of these efforts have been focused on continental shallow earthquakes, but here we introduce an integrated deep-learning-based workflow to detect deep earthquakes recorded by a temporary array of ocean-bottom seismographs (OBSs) and land-based stations in the Tonga subduction zone. We develop a new phase picker, PhaseNet-TF, to detect and pick *P*- and *S*-wave arrivals in the time-frequency domain. The frequency-domain information is critical for analyzing OBS data, particularly the horizontal components, because they are contaminated by signals of ocean-bottom currents and other noise sources in certain frequency bands. PhaseNet-TF shows a much better performance in picking S waves compared to its predecessor PhaseNet. The predicted phases are associated using an improved Gaussian Mixture Model Associator GaMMA-1D and then relocated with a double-difference package teletomoDD. We further enhance the model performance with a semi-supervised learning approach by iteratively refining labelled data and retraining PhaseNet-TF. This approach effectively suppresses false picks and significantly improves the detection of small earthquakes. The new catalogue of Tonga deep earthquakes contains more than 10 times more events compared to the reference catalogue that was analyzed manually. This deep-learning-enhanced catalogue reveals Tonga seismicity in unprecedented detail, and better defines the lateral extent of the double-seismic zone at intermediate depths and the location of 4 large deep-focus earthquakes relative to background seismicity. It also offers new potential for deciphering deep earthquake mechanisms, refining tomographic models, and understanding of subduction processes.

Key words: Machine learning; Seismicity and tectonics; Subduction zone processes; Neural networks; Pacific Ocean

1 INTRODUCTION

Detecting and locating earthquakes in subduction zones plays a pivotal role in advancing the understanding of subduction processes and earthquake physics. In particular, earthquakes deeper than 50 km provide critical information on slab geometry, slab mineral dehydration and transformation, and the interaction between the slab and surrounding mantle (Green & Houston 1995; Zhan 2020). Initial studies, such as Ruff & Kanamori (1980), established meaningful connections between seismicity and physical attributes of subduction zones, such as the lateral extent and penetration depth of the Wadati-Benioff zone, the age of the subducting lithosphere, convergence rates, and back-arc spreading. In recent years, comprehensive global slab models like Slab1.0 (Hayes et al. 2012) and Slab2 (Hayes et al. 2018) have leveraged high-accuracy regional seismicity catalogues to refine slab geometry. Precise earthquake distributions also help reveal the underlying mechanisms of intermediate-depth ($\sim$70–300 km) and deep-focus (300–700 km) earthquakes (Wiens et al. 1993; Brudzinski et al. 2007; Kita et al. 2010; Wei et al. 2017; Chen et al. 2019; Florez & Prieto 2019). However, most global studies suffer from limited local station coverage, especially offshore, and most regional studies with temporary deployments lack sufficient duration, which limits high-precision earthquake locations in large numbers.

Recent advances in the applications of deep learning methods in seismology greatly increase the information content that can be extracted from seismic datasets by detecting many more earthquakes (Mousavi & Beroza 2022, 2023). Initial efforts, such as Gentili & Michelini (2006); Ross et al. (2018), used simple neural networks for detecting seismic phase arrivals, a foundational step in earthquake localization. Subsequent developments incorporated biomedical image segmentation algorithms, notably the U-Net architecture (Ronneberger et al. 2015), to create highly effective deep-neural network (DNN) phase pickers like PhaseNet (Zhu & Beroza 2019). The Transformer architecture (Vaswani et al. 2017) has further inspired new models, such as the EQTransformer (Mousavi et al. 2020), which leverages attention mechanisms to enhance phase detectability. For seismic phase association that links seismic arrivals to preliminary event origins, significant improvements have been achieved through Gaussian mixture models (Zhu et al. 2022) and graph neural networks (GNN) (McBrearty & Beroza 2023). These machine-learning-based techniques outperform traditional methods in both phase-picking (Baer & Kradolfer 1987; Sleeman & van Eck 1999) and phase association (Zhang et al. 2019).

Most machine-learning studies have been focused on continental, shallow earthquakes. Limited attention has been given to deep earthquakes in subduction zones. For instance, PhaseNet and GaMMA were developed using seismic data from Northern California, where most earthquakes occur at depths shallower than 20 km. EQTransformer was trained with the STanford EArthquake Dataset (STEAD)

(Mousavi et al. 2019), which, despite its global scope, contains earthquakes predominantly shallower than 100 km. Generalized Seismic Phase Detection (Ross et al. 2018) is developed with vast hand-labelled data archives of the Southern California Seismic Network, which is also dominated by continental earthquakes. Studies utilizing these methods, (e.g., Chai et al. 2020; Liu et al. 2020; Park et al. 2020; Ross et al. 2020; Tan et al. 2021; Wilding et al. 2023; Liu et al. 2023; Gong et al. 2023) similarly concentrate on continental earthquakes.

Since many subduction zones are covered by oceans, offshore seismic data is critical for investigating subduction zone earthquakes. However, data from ocean-bottom seismographs (OBSs) is generally noisier than that from land-based stations because of ocean-bottom currents, seismometer tilting, instrument coupling, etc. Recent efforts utilize machine-learning packages such as PhaseNet and EQTransformer to process OBS data but show a lower performance compared to continental data (Bornstein et al. 2023).

The Tonga subduction zone hosts abundant intermediate-depth earthquakes and produces the majority of deep-focus earthquakes, and thus serves as a unique natural laboratory for studying deep earthquakes. However, studying Tonga's earthquakes has been challenging. Global catalogues, such as the ISC EHB catalogue, mainly rely on a handful of land-based stations on the islands of Tonga and Fiji. These catalogues provide foundational information on Tonga earthquakes, but the hypocentre precisions, particularly in the vertical direction, are limited due to the lack of local stations. Since 1993, a few temporary seismic deployments, including broadband OBSs, greatly improved the data coverage and earthquake hypocentre precisions in this region, leading to ground-breaking discoveries (Wiens et al. 1993, 1994; Wei et al. 2017). However, the short duration of these deployments has limited the number of analysed earthquakes, and motivates a systematic effort to mine these datasets for more small earthquakes.

Innovative approaches are needed to tackle earthquake detection and location in the Tonga subduction zone. First, the phase picker must be capable of handling noise in OBS data that is sometimes enriched in specific frequency ranges. To solve this problem, we introduce a new phase picker PhaseNet-TF to detect seismic arrivals in the time-frequency domain. Second, the phase associator should be more efficient than the conventional back-projection-based methods and account for the change in seismic velocity with respect to depth. We develop a new associator GaMMA-1D to associate arrivals output from PhaseNet-TF. Finally, given the limited data, optimizing the use of existing data is crucial. Here we build a new semi-supervised learning-based workflow to analyse seismic data from a 1-year temporary deployment.

2 DATA

In this study, we analysed seismic data recorded by a temporary seismic array deployed in the Tonga subduction zone from November 2009 to December 2010 (Figure 1). This array included 49 OBSs (network ID YL) with either Guralp CMG3T_120sec (100 Hz sample rate) or LDEO OBS Sensor Mk2 seismometers (40 Hz sample rate), 17 island-based stations (network ID Z1) with Guralp CMG40T, Streckeisen STS-2, or Nanometrics Trillium 120 seismometers (40 Hz sample rate), and one GSN station MSVF (network ID II) with a Geotech KS-54000 Borehole seismometer (20 Hz sample rate).

We compiled a reference catalogue of local earthquakes, consisting of 1,163 events, 42,256 *P*-wave arrivals, and 14,852 *S*-wave arrivals (Table 1) that were manually picked with the Antelope software (Wei et al. 2017). This catalogue is hereinafter called the manually picked reference catalogue or the reference catalogue. We created a reference dataset by windowing three-component waveforms 5 minutes before and 5 minutes after each *P*-wave arrival. This window is sufficiently long to include the corresponding *S* arrival for the same event. We subsequently removed the instrumental response to obtain displacement waveforms in three components: vertical (Z), east (E or 1), and north (N or 2). We further resample the data to 40 Hz. No additional preprocessing, such as filtering and component rotation, was applied.

We also created a continuous dataset by partitioning the three-component continuous waveforms recorded by this array into 10-day segments and subsequently removing the instrumental response. Since not all stations had complete data from November 2009 to December 2010, we replaced the missing data with zeros. Incomplete components were also accepted, with missing channels filled with zeros. Given the large volume of the data, exceeding 2TB in the miniSEED format, we used the mseedindex package and an ObsPy wrapper (Beyreuther et al. 2010) to construct a miniSEED database. This facilitated efficient data analysis and improved machine learning I/O performance.

3 METHODS

3.1 Phase arrival-time picking by PhaseNet-TF

We develop a new phase picker PhaseNet-TF, based on its predecessor PhaseNet (Zhu & Beroza 2019), to leverage the benefits of the time-frequency domain, which excels in capturing both temporal and spectral features of seismic data. PhaseNet-TF adapts the architecture of DeepLabv3+ (Chen et al. 2018) to accommodate data in the time-frequency domain (Figure 2). DeepLabv3+ is a state-of-the-art semantic image segmentation model that incorporates an encoder-decoder structure to refine object boundaries in segmentation tasks. As part of the renowned DeepLab model series, it offers top-tier performance in a wide array of applications, ranging from autonomous driving to medical image analysis, and outperforms earlier models such as U-Net (Ronneberger et al. 2015), which was used in PhaseNet. A seismic spectrogram acts as an image that represents the time-frequency distribution of phase signal and noise. A spectrogram is generated by applying the short-time Fourier transform (STFT) to three-component time-domain waveforms, and thus consists of 6 components: i.e., the real and imaginary parts of the three-component waveform spectra. Using the spectrogram as an input, DeepLabv3+ produces a pixel-level classification image that matches the dimension of the spectrogram. This output highlights the relative positions of signal and noise and is subsequently processed by a multilayer perceptron to estimate phase and noise probabilities in the time domain.

The manually picked reference dataset is divided into training, validation, and test datasets using stratified sampling, with a distribution ratio of 90:5:5. The ratio for the training dataset is relatively high as we have a limited amount of data. This approach ensures an equitable representation of both *P* and *S* waves, especially given the fact that the number of *S* wave picks is about 1/5 of that of *P* wave picks. The input waveform window is 120 seconds long, with the *P* wave arrival initially centred at the 10-second timestamp. We augment the training dataset in 3 ways. First, we randomly shift the waveform windows to prevent the model from overfitting to specific phase arrival positions. The 10 minute long waveform in our dataset is sufficient for cutting and shifting the 120 seconds window. Second, we randomly stack two signal-bearing windows or one signal-bearing and one noise-only window. The ratio for stacking is fine-tuned as a hyperparameter, allowing the model to adapt to more complex real-world scenarios and preventing it from mistakenly learning that a 120-second window always contains only two phases (*P* and *S*). Third, we stabilize the input data through normalization by subtracting the mean and dividing by the standard deviation of the 120-second window. When applying random stacking, each window is also normalized before stacking, and then the entire stacked waveform is normalized. For the validation and testing sets, we do not shift or stack windows and only stabilize the input data through normalization.

We formulate the training labels to represent the probability of phase arrival times, and use the Kullback-Leibler (KL) divergence for the loss function. The KL divergence differs from the cross-entropy loss used in PhaseNet only by a constant value, so they are equivalent for optimization. We define the probability at time t as follows:

$$y_{\text{true}}(t) = e^{-\frac{(t-t_0)^2}{2\delta^2}}, \quad \text{where} \quad |t - t_0| \leq 3\delta \tag{1}$$

Here, t_0 is the phase arrival time, and δ is the width of the label (20 points, or 0.5 s in our case). This label definition smooths the phase arrival time and allows for the quantification of classification uncertainty through the shape of the model predictions. The KL divergence, measuring the similarity between two probability distributions, is defined as:

$$L(y_{\text{true}}, y_{\text{predict}}) = y_{\text{true}} * \log \frac{y_{\text{true}}}{y_{\text{predict}}} \quad (2)$$

where y_{predict} is the model prediction. A lower KL divergence value indicates a higher similarity between y_{true} and y_{predict}. The KL divergence is evaluated across three output channels: probabilities of *P*, *S*, and noise. The sum of these probabilities is fixed as 1 at each time stamp.

We use the open-source PyTorch library, including AdamW (Loshchilov & Hutter 2019) for optimization and MultiStepLR for learning rate scheduling. AdamW is widely used in computer vision tasks, and deviates from the traditional Adam optimizer by decoupling the weight decay from the gradient update. MultiStepLR adjusts the learning rate at specific epochs, decreasing it by a fixed rate of 0.6 in our case. Our model is trained for 400 epochs, starting with a learning rate of 0.0004, which decays at epochs 15, 30, 45, and 60. We also add an L2 regularization term with a weight decay of 0.001 to the loss function to mitigate overfitting. Early stopping is implemented to prevent overfitting and save computational time. Training is halted if the validation loss does not improve for 30 consecutive epochs. For our reference dataset, the training took about 5 hours on 16 NVIDIA Tesla V100 GPU cards at the MSU HPCC.

We apply the trained PhaseNet-TF model to the continuous dataset for phase detection. The output is continuous probability distributions for *P* waves, *S* waves, and noise. We first partition the continuous waveforms into 120-second segments with a 60-second overlap between consecutive segments. Each segment is normalized in the same way used for model training. Then we apply the model to the entire continuous dataset, which took 16 hours on 4 NVIDIA Tesla V100 GPUs to process. The output is 120-second segments of probability distributions for *P* wave, *S* wave, and noise. We combine these 120-second segments into a single continuous time series by taking the final output probability as the maximum value from the overlapping predictions. Peak probabilities larger than 0.5 are counted as positive picks.

3.2 Phase association by GaMMA-1D

Associating phase picks to specific earthquakes is necessary for locating events and eliminating unreliable picks. We use GaMMA-1D, a Bayesian Gaussian Mixture Model Associator with a 1D velocity structure, which is an improved version of GaMMA (Zhu et al. 2022). While GaMMA-1D retains the Gaussian mixture model framework of its predecessor GaMMA for phase association, it improves calculating phase arrival times by using a fast-sweeping method to solve the Eikonal equation based on a 1D velocity model AK135 (Kennett et al. 1995). In contrast to GaMMA which used a uniform half-space for arrival time predictions, Gamma-1D uses a 1D velocity model, which is critical for the large depth range of earthquakes in Tonga. Events associated with less than 10 picks are discarded. Figure 3 shows the association results for a densely packed sequence of phase picks.

3.3 Earthquake relocation by teletomoDD

We use teletomoDD (Pesicek et al. 2010), a package for double-difference seismic tomography and relocation, to relocate all events associated with GaMMA-1D in the previous step. The 3D seismic velocity model is fixed during inversions and is adopted from the TX2019slab model (Lu et al. 2019). We apply a bootstrap resampling technique to estimate relocation uncertainties and filter out events with large uncertainties. We create 1,000 subsets of the data by randomly excludes 30% of the stations from each subset. After relocating events in these 1,000 subsets, we compute the mean and standard deviation of the hypocentre and origin time of each event. We eliminate events with a standard deviation in longitude and latitude greater than 0.1 degrees, in depth of greater than 10 km, or in origin time of greater than 1 second. This approach effectively removes unreliable picks from PhaseNet-TF and GaMMA-1D as well as events that are poorly constrained. The relocation output catalogue contains the hypocentres and origin times of the remaining events and the corresponding *P*- and *S*-wave arrival times.

3.4 Semi-supervised-learning-based workflow

Since there are only 1,163 manually picked events out of presumably tens of thousands of earthquakes in the Tonga subduction, the reference catalogue and dataset may limit phase detection capability. Therefore, we utilize a semi-supervised learning strategy to iteratively refine labelled picks and retrain PhaseNet-TF (Figure 4). This approach integrates a limited labelled dataset with a larger pool of unlabeled data for model training. In Iteration #1, we train PhaseNet-TF with the original labelled dataset, i.e., the manually picked reference dataset. This model is then applied to the continuous dataset, generating new phase picks that may include false detections. The subsequent steps of phase association by GaMMA-1D and event relocation by teletomoDD filter out unreliable picks and events with large uncertainties. Compared to the reference catalogue, the output catalogue thus contains a larger number of reliable picks. Similar to the reference dataset, we create a new labelled dataset by windowing three-component waveforms 5 minutes before and 5 minutes after each *P* wave arrival from the output catalogue. This newly labelled dataset is divided into the training, validation, and test datasets at a ratio of 90:5:5 to train the PhaseNet-TF model in the next iteration. As more picks predicted by deep learning are added to the training dataset, one can expect more picks and events to be detected, at the cost of increasing arrival time residuals compared to the reference dataset. We continue this iterative workflow for several iterations until the number of events reaches a plateau and the arrival time residuals do not increase dramatically.

4 RESULTS

4.1 PhaseNet-TF model assessment

We assess the PhaseNet-TF model in each semi-supervised-learning iteration using the test dataset, which is 5% of the labelled dataset in the corresponding iteration (Table 2). The evaluation metrics include precision, recall, F1 score, and arrival-time residuals compared to the labelled catalogue. This labelled catalogue is the manually picked reference catalogue for Iteration #1 and is the output catalogue from the previous iteration for Iteration #2 and #3. Predicted picks with arrival-time residuals smaller than 1 second are considered true positives, whereas predicted picks with larger arrival-time residuals are false positives. Labelled picks that are not predicted by PhaseNet-TF are considered false negatives. Precision, recall, and F1 score are defined as

$$\text{Precision: } P = \frac{T_P}{T_P + F_P} \tag{3}$$

$$\text{Recall: } R = \frac{T_P}{T_P + F_N} \tag{4}$$

$$\text{F1: } F1 = \frac{2PR}{P + R} \tag{5}$$

where T_P, F_P, and F_N are the numbers of true positives, false positives, and false negatives, respectively.

In Iteration #1, the PhaseNet-TF output is evaluated against the manually picked reference catalogue. For the *P* wave, the model exhibited a precision of 0.99, a recall of 0.99, and an F1 score of 0.99. For the *S* wave, the corresponding values are 0.97, 0.99, and 0.98, respectively. Figure 5 shows examples of seismograms, spectrograms, and prediction probabilities from iteration #1 at 2 OBSs and 2 land-based stations. In the following iterations, the evaluation metrics remain at the same high level, validating the semi-supervised learning approach and the robustness of PhaseNet-TF in accurately identifying phase arrivals.

4.2 Phase association and earthquake relocation assessments

Phase association and earthquake relocation serve as critical filters for eliminating unreliable predicted picks and poorly constrained events. When manual picks are associated with GaMMA-1D, some of them are missed in the association catalogue and considered false negative picks. The picks associated with GaMMA-1D are subsequently used for event relocation by teletomoDD with bootstrap resampling. Events with large uncertainties and their corresponding picks are discarded during the relocation process. We assess these processes (Table 3) using the reference catalogue that contains manual picks associated with the Antelope software (Wei et al. 2017). When comparing the reference catalogue and the output catalogue by GaMMA-1D or teletomoDD, events with origin-time residuals smaller than 15 seconds are considered true positive events, whereas events with larger origin-time residuals are false positives. If some picks that were associated with a single event by Antelope are associated with multiple events by GaMMA-1D, the new events are also counted as false positives. Because there are no picks added during this processing, the recall for *P*- or *S*-wave arrivals reflects the picks eliminated during association and relocation, and a high recall value is desired. In contrast, new events may be added during the association process, lowering precision, whereas existing events may be discarded during the association and relocation processes, lowering recall. Thus, the F1 score for events that balance precision and recall serves as a better indicator of the filtering performance.

As shown in Table 3, the recall for *P*-wave arrivals is 0.97 after association and 0.95 after relocation, suggesting that GaMMA-1D and teletomoDD are highly effective in retaining manually picked *P*-wave arrivals. However, the recall for *S*-wave arrivals is 0.92 after association and 0.86 after relocation. These numbers indicate that about 8% of the manually picked *S*-wave arrivals are not successfully associated with GaMMA-1D, which impacts the subsequent relocation performance. This could be attributed to either the limitations of GaMMA-1D in associating *S*-wave arrivals or inaccurate manual *S*-wave picks. Nonetheless, the overall performance of the association and relocation filtering processes remains promising.

4.3 Phase detection and event relocation on continuous data

In Iteration #1, the PhaseNet-TF model is trained by the manually picked reference dataset. When applying this model to the continuous data, PhaseNet-TF detects 294,050 *P*-wave arrivals and 112,547 *S*-wave arrivals, which is substantially more than the number of picks in the reference catalogue. Figure 6 demonstrates the performance on one hour of continuous data. These arrivals are associated with GaMMA-1D in a preliminary catalogue. In this step, about 10% of *P*- and 30% of *S*-wave arrivals are discarded, and the associated catalogue consists of 13,111 events with 265,439 *P*-wave , and 79,380 *S*-wave arrivals. These events generally align with the reference catalogue but are more scattered (Figures 7a, 7b, 8a, and 8b). Many events in the mantle wedge are not reliable as they they have a large azimuthal coverage gap. The subsequent relocation and error estimation filter out most of these outlier events, leaving a new catalogue of 9,427 events with 217,254 *P*-wave, and 63,590 *S*-wave arrivals (Figures. 7c and 8c, Table 1). When comparing this catalogue with the reference catalogue, the recall for *P*-waves, *S*-waves, and events are 0.94, 0.83, and 0.96, respectively, and the standard deviations of arrival-time residuals are 0.14 and 0.15 seconds for *P* and *S* waves, respectively (Figures 9a and 9b), suggesting that our workflow can effectively detect seismic arrivals and earthquakes that were manually picked. More importantly, the new catalogue contains dramatically more *P*- and *S*-wave arrivals and events (Table 1).

Leveraging this new catalogue, we assemble a new labelled dataset enriched with phase arrivals detected in Iteration #1 of the semi-supervised learning workflow. This new dataset (120 GB) is substantially larger than our initial reference dataset (22 GB). The increased dataset size requires additional computational resources, extending the training time from 5 to 24 hours while utilizing the same number of GPUs. In Iteration #2, this new PhaseNet-TF model is applied to the continuous dataset again, resulting in significantly more arrivals and events (Figures. 7d and 8d). The standard deviation of arrival-time residuals for *P* waves remains 0.15 seconds (Figure 9c), but that for *S* waves increases from 0.15 to 0.23 seconds (Figure 9d). In Iteration #3 which uses the output catalogue from Iteration #2 for training, the numbers of arrivals and events and arrival-time residuals remain stable (Figs. 7e and 8e). We thus cease the semi-supervised learning workflow after Iteration #3, anticipating diminishing returns in further iterations.

Our final catalogue from Iteration #3 contains 13,406 relocated events with 372,774 *P*-wave arrivals and 78,853 *S*-wave arrivals. Compared with the manually picked reference catalogue, our final compilation boasts a factor of 11 times more events, 8 times more *P*-wave phases, and 5 times more *S*-wave phases. Figures 7 and 8 show that our final catalogue offers enhanced delineation of both the slab geometry and double seismic zone, demonstrating its superiority over the reference catalogue.

5 DISCUSSION

5.1 Comparison with previous packages

In this study, PhaseNet-TF detects seismic arrivals in the time-frequency domain, different from most other deep-learning phase pickers that work in the time domain. Using a manually picked reference catalogue and dataset, we conduct a quantitative and fair comparison between PhaseNet and PhaseNet-TF. We first test the original PhaseNet model that was trained by the Northern California data (Zhu & Beroza 2019). We also retrain the PhaseNet architecture with our training dataset from Tonga. The PhaseNet-TF model in Iteration #1 is used for comparison. All models are evaluated on the same testing dataset to ensure a fair comparison.

Table 2 highlights the superiority of PhaseNet-TF over PhaseNet in detecting seismic arrivals, particularly for OBS data. PhaseNet with its original weights shows poor performance for both *P* and *S* waves. This is an unsurprising outcome given that it was trained with a dataset from a different tectonic setting and on land-based vs. OBS instruments. When retrained with the Tonga dataset, PhaseNet's performance is similar to PhaseNet-TF for detecting *P*-wave arrivals but displays a lower performance for *S* waves. Furthermore, the standard deviation of *S*-waves arrival-time residuals for PhaseNet-TF (Iteration #1) are significantly smaller than those for PhaseNet models (Fig. 9b and 9h). These differences indicate that including the time-frequency domain and the new architecture enhances the model's capability to detect *S* waves. This is because the horizontal components that record *S* waves are much noisier for OBS data compared to land-based stations, due to seismometer tilting and ocean-bottom currents (Webb & Crawford 1999; Wei et al. 2015).

For associating seismic arrivals from Tonga deep earthquakes, GaMMA-1D exhibits higher performance compared to GaMMA, which was designed for California (Zhu et al. 2022). That is because GaMMA-1D uses a 1D velocity model AK135, whereas GaMMA assumes a uniform velocity model. We test both GaMMA and GaMMA-1D to associate all manual picks and compare the output catalogues against the reference catalogue. When comparing the origin-time and depth residuals, GaMMA-1D consistently achieves superior accuracy to its predecessor GaMMA (Figure 10). Table 3 lists the evaluation metrics for GaMMA-1D and GaMMA. Compared to GaMMA, GaMMA-1D achieves a similar performance for associating P- and S-wave picks to certain events. However, the low precision of event association (0.76) suggests that GaMMA tends to break a single event into multiple events. This problem will impact the next step of earthquake relocation, resulting in more events with poorer constraints and/or misassociated phases.

Our workflow is readily adaptable to a cloud computing setting through modifications to the machine learning models employed in Quakeflow (Zhu et al. 2023). Quakeflow is a cloud-based earthquake monitoring system designed for detecting seismic activity and analyzing source characteristics from continuous waveform data. It currently utilizes PhaseNet for phase picking, GaMMA for phase association, and HypoDD for event relocation. Given the compatibility in model inputs and outputs, these can be smoothly swapped with PhaseNet-TF, GaMMA-1D, and teletomoDD. A future version of Quakeflow potentially provides an efficient and effective solution for enhancing real-time earthquake surveillance and for in-depth analysis of historical seismic data, particularly for deep earthquakes in subduction zones and OBS data.

5.2 Tonga deep earthquakes revealed by the new catalogue

With only 1 year of data, our results show unprecedented detail in the Wadati-Benioff zone. Figure 11 compares the new catalogue against the manually picked reference catalogue (Wei et al. 2017) and the ISC EHB Bulletin from 1964 to 2020 (International-Seismological-Centre 2023). The latter uses the

EHB algorithm (Engdahl et al. 1998) to minimize hypocentre errors, particularly in the vertical direction, and is arguably the most precise global catalogue. The general pattern of earthquake distribution remains similar across all catalogues.

Double seismic zones (DSZs), in which intermediate-depths earthquakes occur along two planes parallel to the dip of the slab, are observed in many subduction zones, and are attributed to metamorphic reactions that release fluids or volatiles in the slab (e.g., Hacker et al. 2003; Yamasaki & Seno 2003; Brudzinski et al. 2007). The Tonga DSZ was initially discovered by Kawakatsu (1985) using focal mechanisms constrained by global data. Using the 2009-2010 temporary deployment, Wei et al. (2017) confirmed the existence of the Tonga DSZ and revealed more details. Our new catalogue shows a much clearer DSZ along cross-section B-B' that extends to about 300 km depth. Although hinted by Wei et al. (2017), the new results explicitly suggest that the lower plane of the DSZ is confined between the latitudes of 19°S and 21°S (the cyan box in Figure 11a), diminishing to the north and south. A DSZ with a limited extent in Tonga is in agreement with similar observations in Japan (Igarashi et al. 2001) and Alaska (Wei et al. 2021), suggesting that deeper parts of the slab mantle are not uniformly hydrated. We do not observe a deeper DSZ at 350–460 km depths that was interpreted as the edges of a metastable olivine wedge in the slab (Wiens et al. 1993). This could be because there were not enough earthquakes occurring at these depths during the 1-year deployment to delineate that feature.

The Tonga subduction zone hosts the majority of deep-focus earthquakes in the world, including 4 notable large events: Mw 7.6 on 9 March 1994, Mw 7.3 on 9 November 2009, Mw 8.2 on 19 August 2018, and Mw 7.9 on 6 September 2018. Our results show that the 1994 Mw 7.6 and 2018 Mw 8.2 events occurred at the bottom of a highly seismogenic region (Figure 11d), consistent with the previous suggestion that these events initiated rupturing in the cold slab (McGuire et al. 1997; Fan et al. 2019). In contrast, the 2018 Mw 7.9 event occurred in a previously aseismic region (Fig. 11g), possibly rupturing through a dissipative process at the edge of a warm fossil slab (Fan et al. 2019; Jia et al. 2020). The 2009 Mw 7.3 event occurred at the western end of a seismicity band corresponding to a fossil slab subducted at the now inactive Vitiaz Trench (Cai & Wiens 2016).

6 CONCLUSIONS

Our integrated workflow has proven highly effective at detecting and locating deep earthquakes in the Tonga subduction zone. We use PhaseNet-TF to detect *P*- and *S*-wave arrivals in the time-frequency domain, showing superior performance over traditional ways of picking arrivals in the time domain. Detecting arrivals in the time-frequency domain is critical for analysing OBS data, particularly the horizontal components with much higher noise levels compared with land-based stations. We use GaMMA-1D to associate arrivals, teletomoDD to relocate events, and a bootstrap resampling approach to estimate uncertainties. This workflow effectively removes artificial arrivals and events with poor constraints. Furthermore, through semi-supervised learning, the PhaseNet-TF model improves iteratively, leading to a more comprehensive and accurate earthquake catalogue compared to the initial manual picks.

This research opens new avenues for in-depth studies in subduction zones, particularly those with limited local data coverage like Tonga. The new catalogue with more events and arrivals potentially benefits future work of high-resolution tomography imaging and earthquake similarity analyses, helping us better understand deep earthquake mechanisms and subduction processes. While our study focuses on Tonga, the methods and workflow are readily adaptable for application in other subduction zones, offering a versatile tool for both real-time monitoring and historical data analyses.

ACKNOWLEDGMENTS

We thank D. A. Wiens for constructive discussions. This research was made possible by the support of National Science Foundation grants EAR-1942431 and OCE-1928946 to S.S.W.. S.S.W. and N.S. were also supported by the Michigan State University Geological Sciences Endowment. We extend our gratitude to the Extreme Science and Engineering Discovery Environment (XSEDE) funded by NSF Grant ACI-1053575. Computing resources were made available through XSEDE Grant TG-EAR140030, hosted on the Expanse supercomputer at the San Diego Supercomputer Center, University of California, San Diego. We acknowledge the evolution from XSEDE to the Advanced Cyberinfrastructure Coordination Ecosystem: Services & Support (ACCESS), and appreciate their ongoing dedication to facilitating valuable cyberinfrastructure resources for researchers. Additional computational support was provided by the Institute for Cyber-Enabled Research (ICER) at Michigan State University.

DATA AVAILABILITY

All data and codes associated with this study are publicly accessible and built upon open-source platforms. PhaseNet-TF can be accessed via its GitHub repository: https://github.com/ziyixi/PhaseNet-TF, and GaMMA-1D is available at https://github.com/AI4EPS/GaMMA. PhaseNet and GaMMA packages are available at their respective GitHub repositories: https://github.com/AI4EPS/PhaseNet and https://github.com/AI4EPS/GaMMA (the same as GaMMA-1D). More specifically, the PhaseNet-TF model weights for Tonga deep earthquakes are available at https://github.com/ziyixi/PhaseNet-TF/releases/tag/v0.3.0.

Data processing and visualization are conducted using open-source Python packages, including

ObsPy (https://github.com/obspy/obspy/) and PyGMT (https://github.com/GenericMappingTools/pygmt). Seismic data in this research are archived at the EarthScope/IRIS Data Management Center under network codes YL, II, and Z1.

Table 1. Numbers of picks and events in the manually picked reference catalogue and output catalogues. Recalls are evaluated against the reference catalogue. The picks with arrival-time residuals < 1 s compared to the reference catalogue are counted as true positive picks, whereas the events with origin-time residuals < 15 s are considered true positive events. The output catalogue of Iteration #3 is considered the final catalogue. The low recall values of *S*-wave arrivals result from the filtering processes of phase association and relocation, as many *S*-wave arrivals are discarded.

	P-wave arrival		*S*-wave arrival		Event	
	Recall	Number	Recall	Number	Recall	Number
Reference	N/A	42,256	N/A	14,852	N/A	1,163
Iteration #1 output	0.94	217,254	0.83	63,590	0.96	9,427
Iteration #2 output	0.94	343,247	0.80	79,593	0.96	13,799
Iteration #3 output (Final)	0.89	372,774	0.75	78,853	0.91	13,406

Table 2. Evaluation metrics of phase pickers on the test dataset for different architectures and models. Picks with arrival-time residuals < 1 s compared to the manually picked reference catalogue are counted as true positive picks. The metrics in the table are evaluated on the test dataset partitioned from the labelled dataset, which is the manually picked reference catalogue for PhaseNet-TF Iteration #1 and two PhaseNet models, and the output catalogue from the previous iteration for PhaseNet-TF Iterations #2 and #3.

	P-wave arrival			*S*-wave arrival		
	Precision	Recall	F1	Precision	Recall	F1
PhaseNet-TF (Iteration #1)	0.99	0.99	0.99	0.97	0.99	0.98
PhaseNet-TF (Iteration #2)	0.99	0.99	0.99	0.96	0.99	0.98
PhaseNet-TF (Iteration #3)	0.99	0.98	0.99	0.96	0.99	0.98
PhaseNet retrained by the Tonga dataset	0.97	0.97	0.97	0.85	0.94	0.90
PhaseNet with original model weights (trained with Northern California data)	0.89	0.66	0.76	0.48	0.28	0.36

Table 3. Evaluation of association and relocation filtering on the manually picked reference catalogue (Iteration #1). Events with origin time residuals < 15 s are counted as true positive events, and phase arrival-time residuals < 1 s are counted as true positive picks.

	P-wave arrival	*S*-wave arrival	Event		
	Recall	Recall	Precision	Recall	F1
Association by GaMMA-1D	0.97	0.92	0.97	0.98	0.97
Relocation using GaMMA-1D output and filtering (epicentre uncertainty $< 0.1°$, depth uncertainty < 10 km, and origin-time uncertainty < 1 s)	0.95	0.86	0.98	0.95	0.96
Association by GaMMA	0.97	0.91	0.76	0.96	0.85

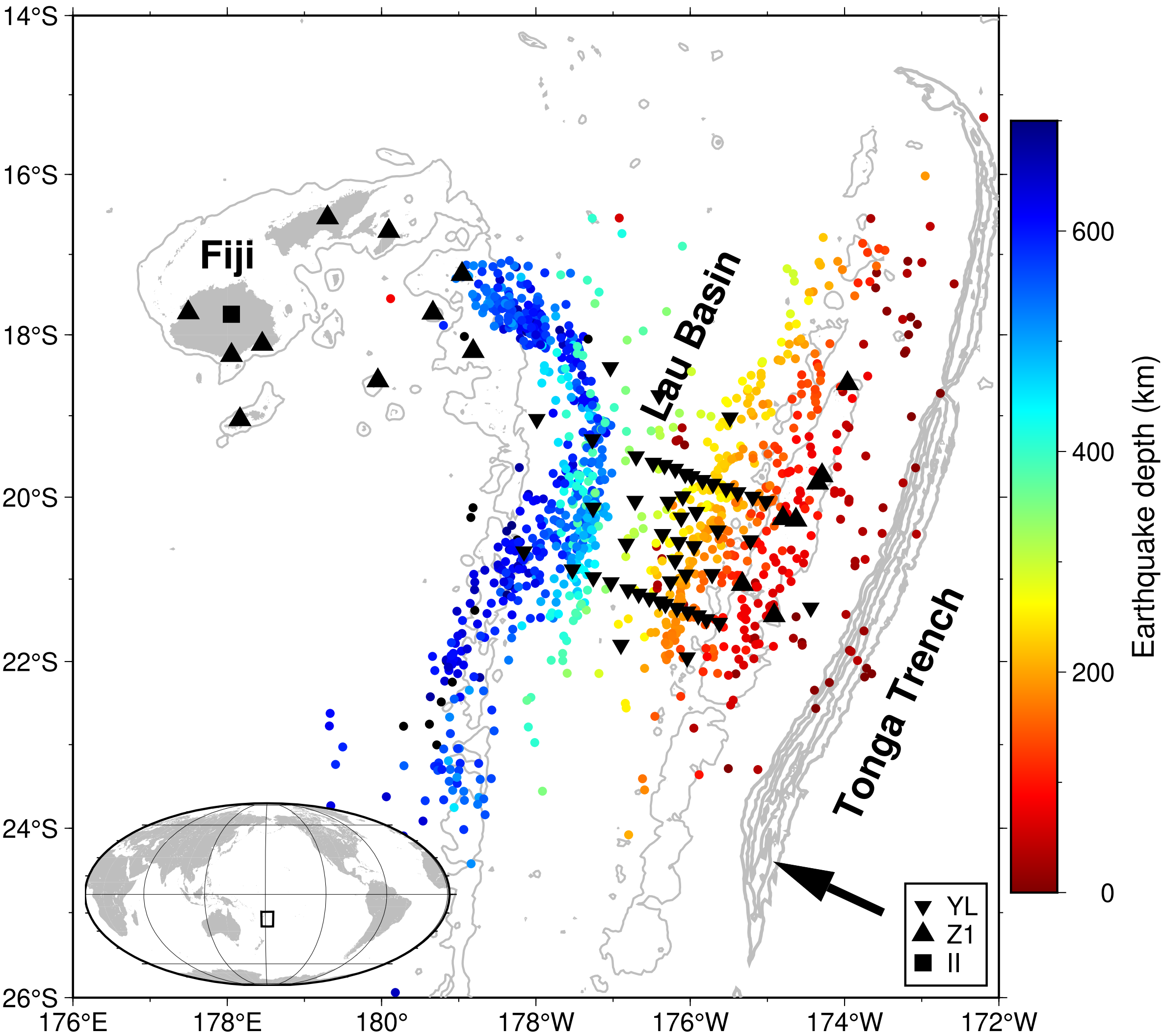

Figure 1. Map of the Tonga subduction zone and adjacent regions. Earthquakes in the manually picked reference catalogue are shown as dots colour-coded by depth. Black triangles, inverted triangles, and square represent land-based stations, ocean-bottom seismographs, and a GSN station, respectively, deployed from November 2009 to December 2010. Land areas are shaded in grey. The bathymetry contours of 1 km highlight features such as the Tonga Ridge, Lau Ridge, and Fiji Plateau. Additional bathymetry contours at 7, 8, 9, and 10 km delineate the Tonga Trench. Black arrow indicates the Pacific Plate's motion relative to Tonga. Inset provides a global context for the study region.

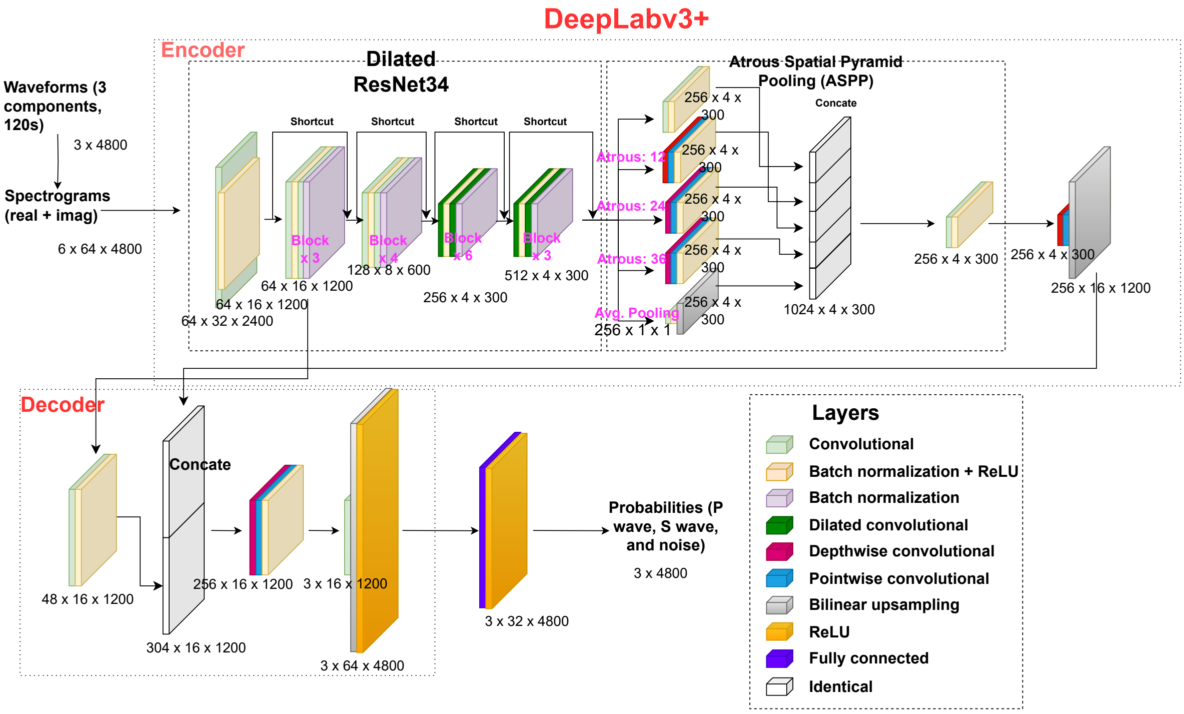

Figure 2. PhaseNet-TF architecture. The input consists of 120-second three-component seismograms with a sample rate of 40 Hz, so the input has a dimension of 3×4800. The output includes three probability time series, corresponding to *P*-wave arrival, *S*-wave arrival, and noise, with the same length as the input. Dimensions for each layer are denoted adjacent to the layer, with the format of ”number of channels × layer height × layer width”. The input seismograms are first transformed into spectrograms before being processed through the DeepLabv3+ network. DeepLabv3+ includes an encoder and a decoder and is equipped with skip layers. The decoder features a dilated ResNet34 and Atrous Spatial Pyramid Pooling (ASPP). The output of DeepLabv3+ is subsequently refined through a multilayer perceptron.

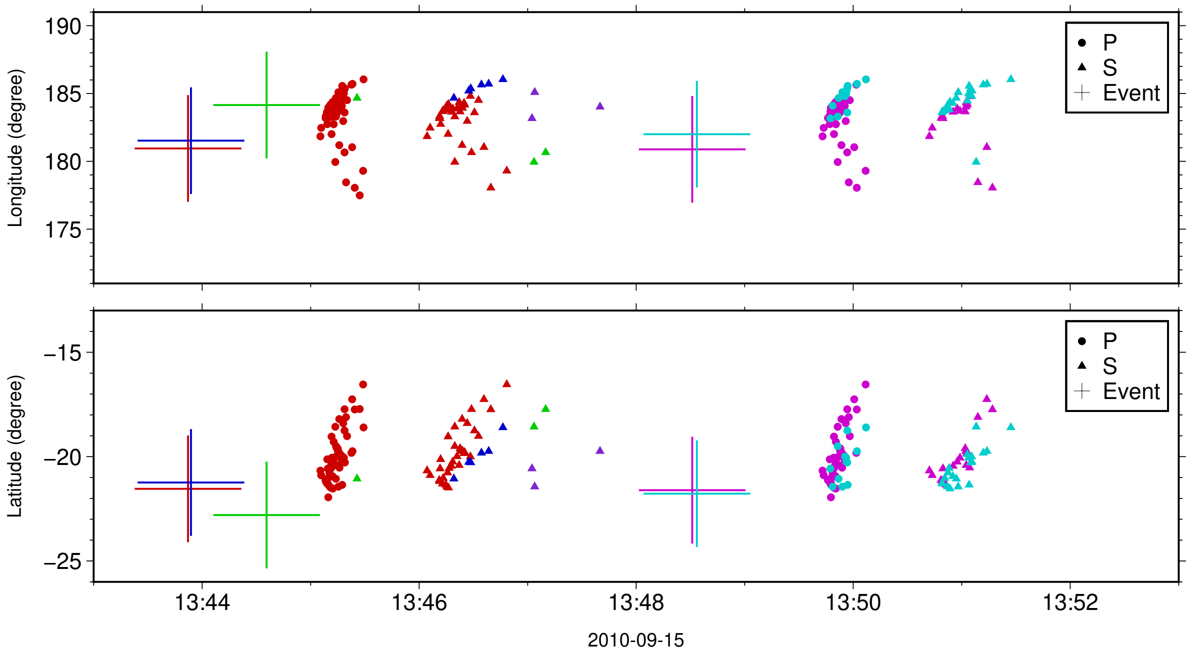

Figure 3. Examples of GaMMA-1D association from UTC 13:43 to 13:53 on September 15, 2010. The top panel shows associated arrivals with respect to longitude, whereas the bottom panel shows them against latitude. In both panels, individual colours denote distinct associated events. Dots and triangles indicate *P*- and *S*-wave arrivals, respectively, while crosses mark the origin time and locations of the associated events. Events associated with less than 10 phase arrivals (e.g., the green-coloured event and arrivals) will be discarded in the following step.

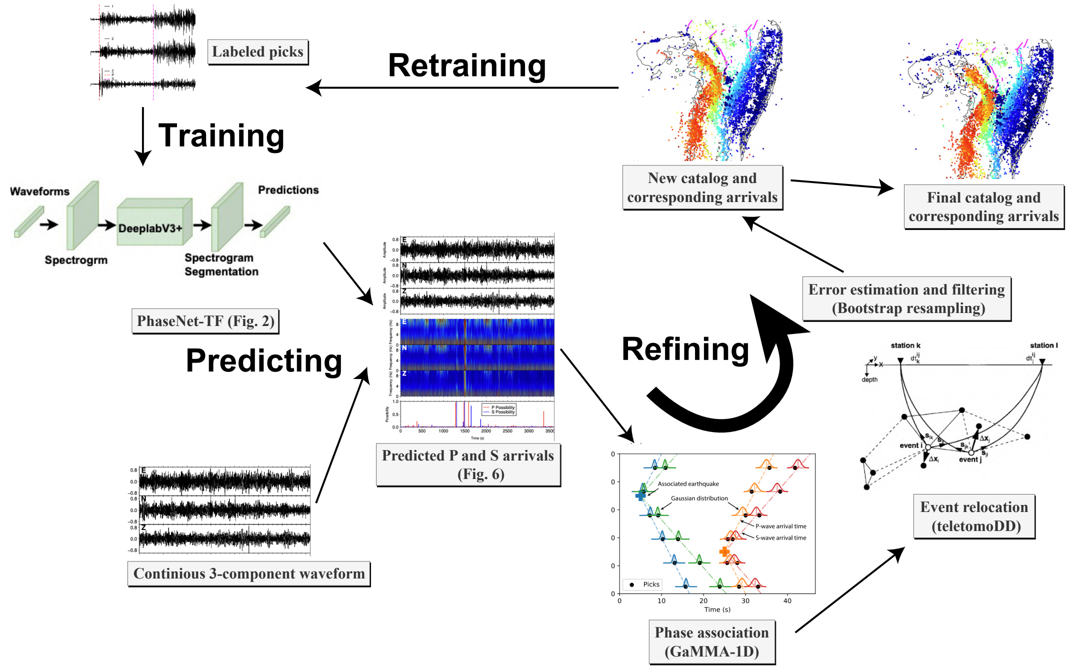

Figure 4. Schematic of our semi-supervised learning workflow. The process begins with training the PhaseNet-TF model using manually picked arrivals. The trained model is then applied to continuous seismic data to obtain *P*- and *S*-wave arrival probabilities. The following phase association by GaMMA-1D, event relocation by teletomoDD, and error estimation/filtering with a bootstrap resampling approach together produce a refined event catalogue and associated phase arrivals. This updated catalogue serves as a new labelled dataset for training and validating PhaseNet-TF in the next iteration. The entire workflow is iteratively repeated until no significant improvements are observed, culminating in the final event catalogue and corresponding phase arrivals.

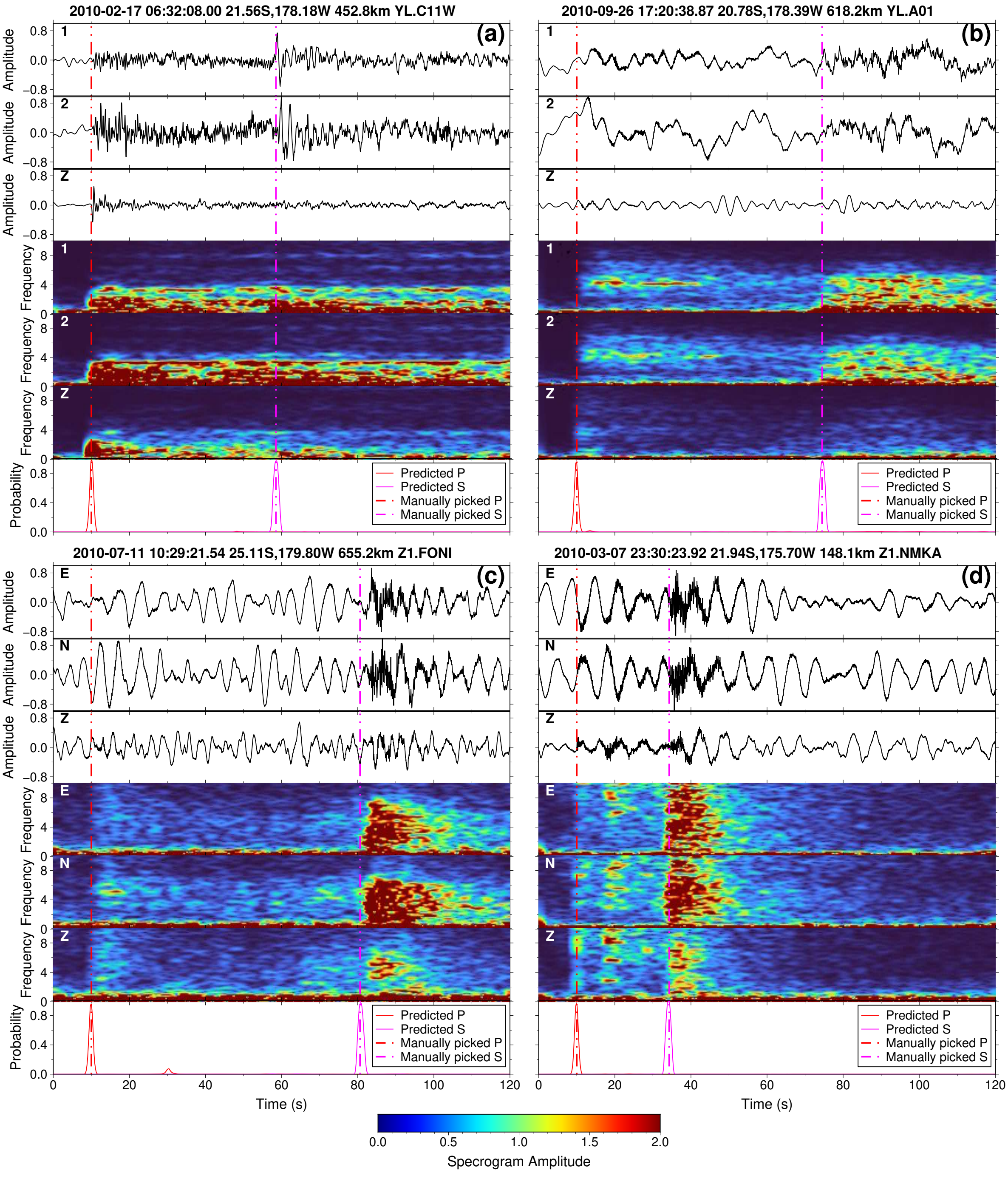

Figure 5. Examples of PhaseNet-TF prediction on the test dataset. (a) and (b) show deep earthquakes recorded at OBSs, whereas (c) and (d) show events recorded at land-based stations. In each panel, the title includes the origin time, hypocenter, and station name. The top 3 sections display the three-component waveforms in the time domain, followed by 3 sections of spectrograms (power value) of the three components. The bottom section shows the probabilities of predicted *P*- and *S*-wave arrivals. Manually picked *P*- and *S*-wave arrivals are indicated by dashed lines.

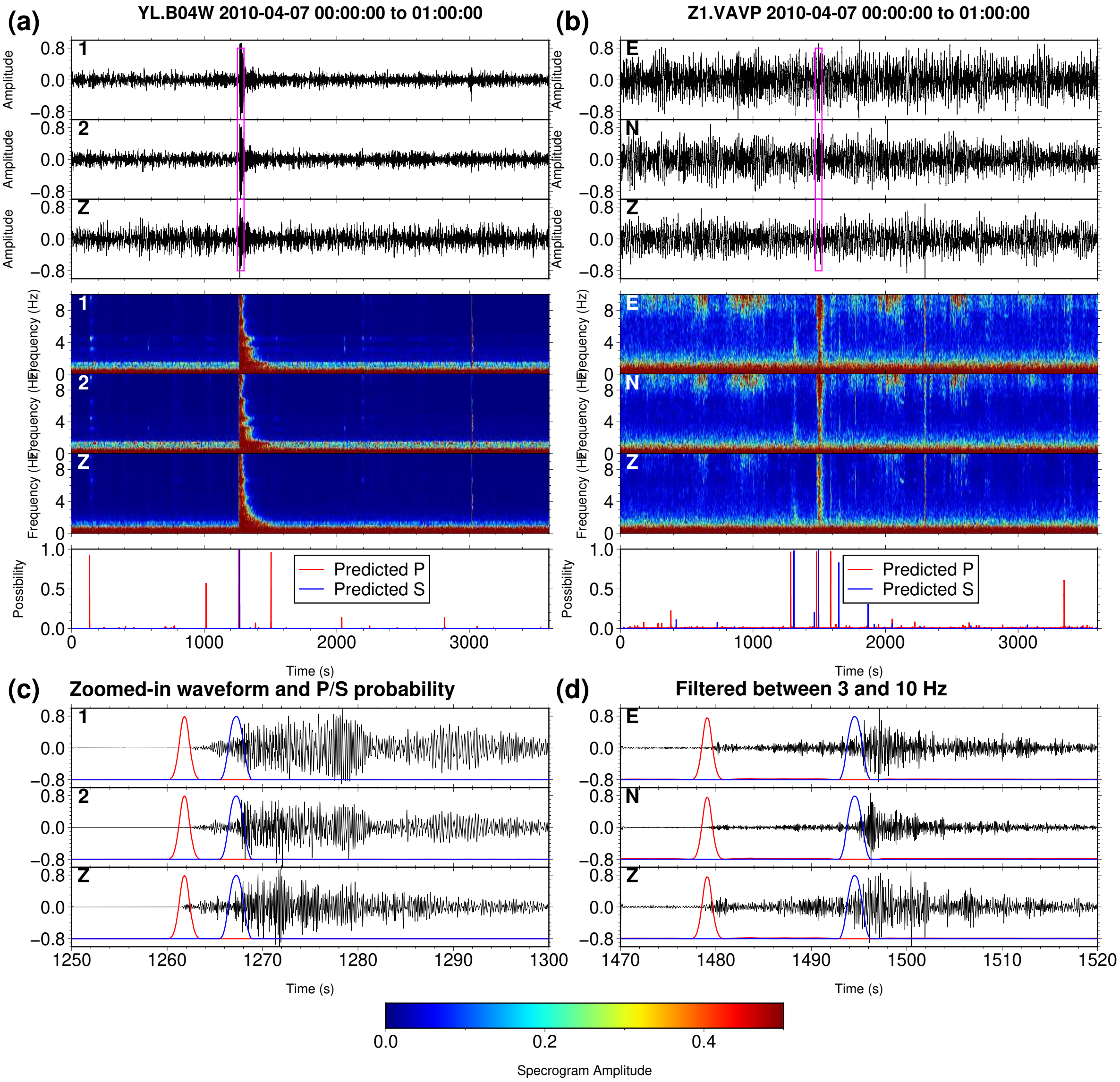

Figure 6. Examples of PhaseNet-TF prediction on continuous data from UTC 00:00 to 01:00 on 7 April 2010 on an OBS B04W (a) and a land-based station VAVP (b). (a) and (b) are similar to Figure 5, except that there are no manual picks. (c) Zoomed-in waveform filtered at 3-10 Hz and *P*/*S* probability within the time window indicated by the magenta box in (a). (d) Zoomed-in waveform filtered at 3-10 Hz and *P*/*S* probability within the time window indicated by the magenta box in (b). The *P* and *S* arrivals are confirmed to be true by the following steps of phase association and event relocation.

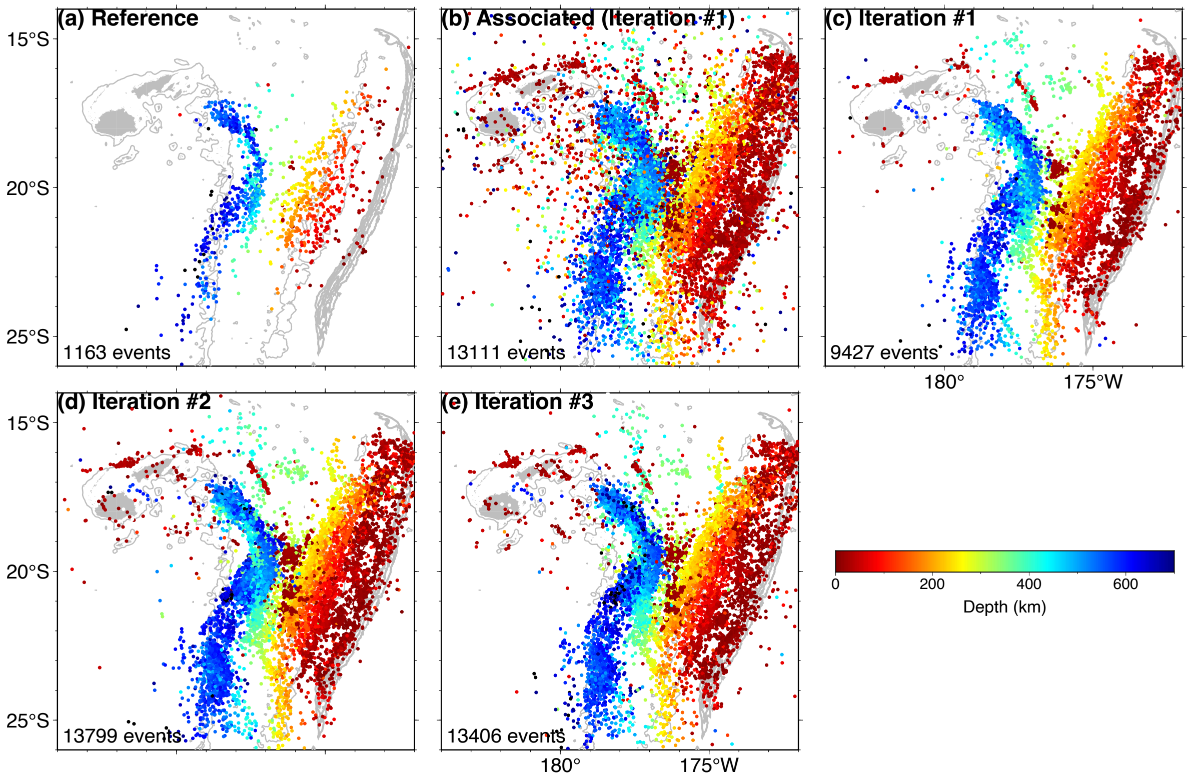

Figure 7. Maps of event distributions at various stages of the analysis. (a) The manually picked reference catalogue by Wei et al. (2017). (b) Events predicted by PhaseNet-TF and associated by GaMMA-1D in Iteration #1. (c) Relocated events serve as the output catalogue of Iteration #1. (d) Output catalogue of Iteration #2. (e) Output catalogue of Iteration #3, considered the final catalogue. All panels are plotted similarly to Figure 1. The number of events for each step is shown in the bottom-left corner of each panel.

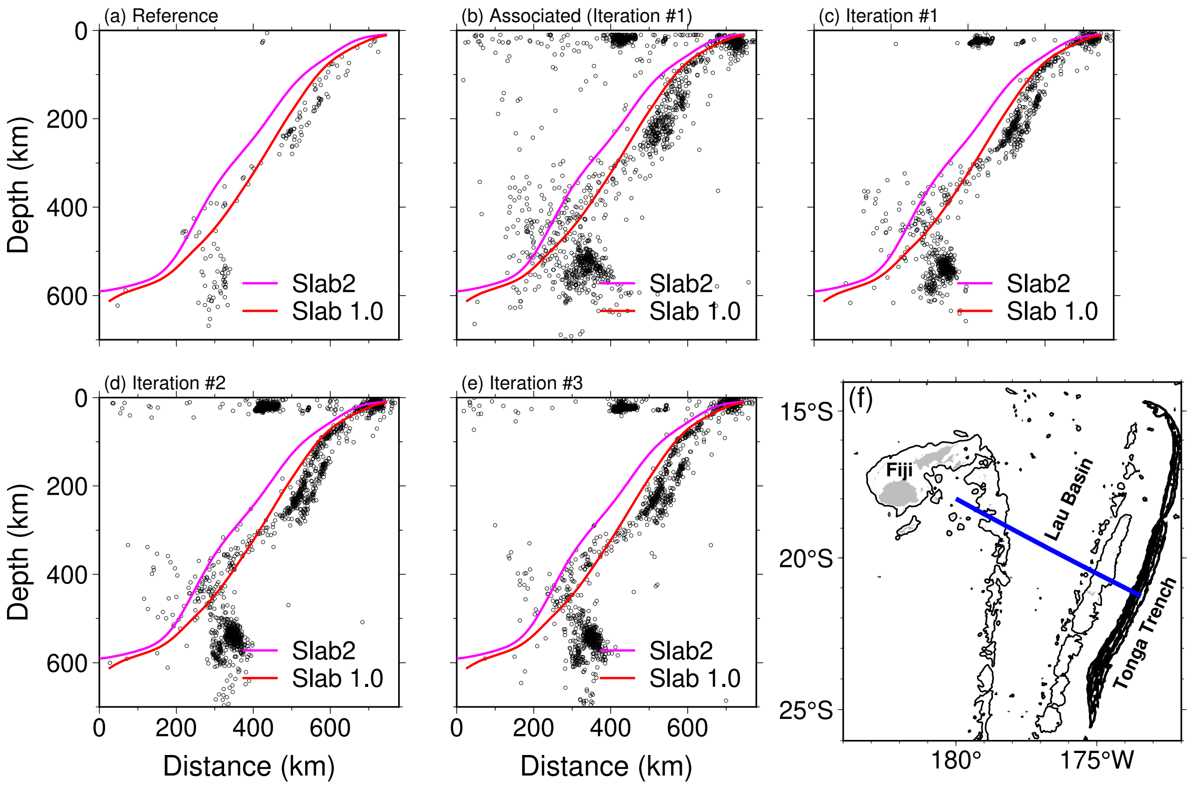

Figure 8. Cross-sections of event distributions at various stages of the analysis. (a) The manually picked reference catalogue by Wei et al. (2017). (b) Events predicted by PhaseNet-TF and associated by GaMMA-1D in Iteration #1. (c) Relocated events serve as the output catalogue of Iteration #1. (d) Output catalogue of Iteration #2. (e) Output catalogue of Iteration #3, considered the final catalogue. (f) The location of the cross-section (blue line). In each of (a) – (e), black circles indicate earthquakes within 70 km away from the cross-section. Red and magenta curves shows the slab upper interface according to the Slab1.0 (Hayes et al. 2012) and Slab2 (Hayes et al. 2018) models, respectively. Neither of these models is accurate in the Tonga subduction zone.

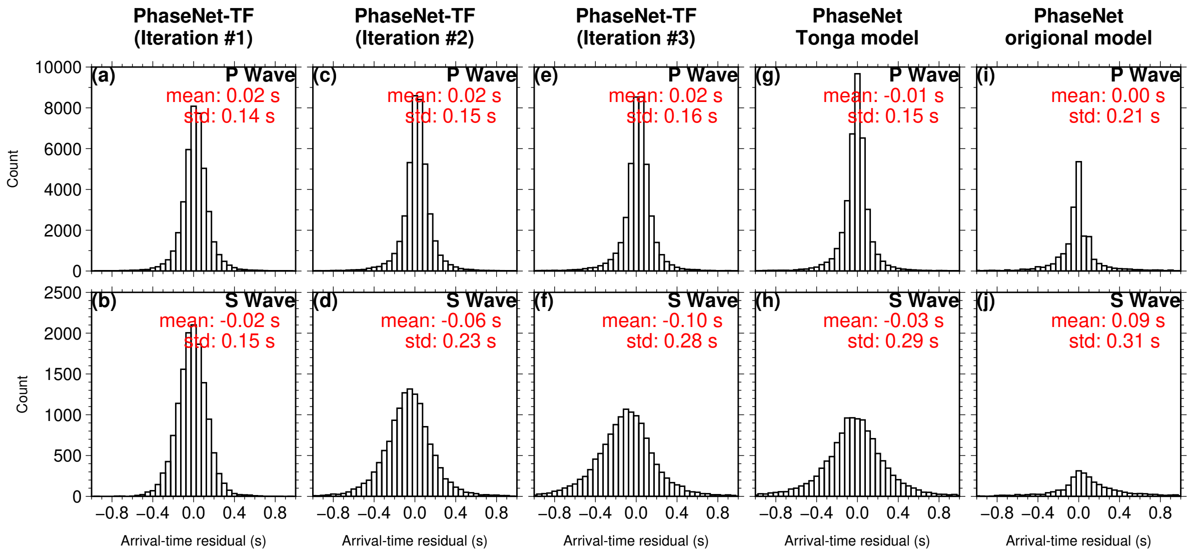

Figure 9. Arrival-time residuals of *P* (top) and *S* (bottom) waves across different models and iterations. When each model is applied to the continuous dataset, the predicted arrivals are compared to manual picks when they exist, and the arrival-time differences contribute to the histogram. (a-f) Results of PhaseNet-TF from three consecutive iterations. (g-h) Outcomes of PhaseNet retrained with the Tonga dataset. (i-j) Results of PhaseNet with its original model weights trained with data from Northern California.

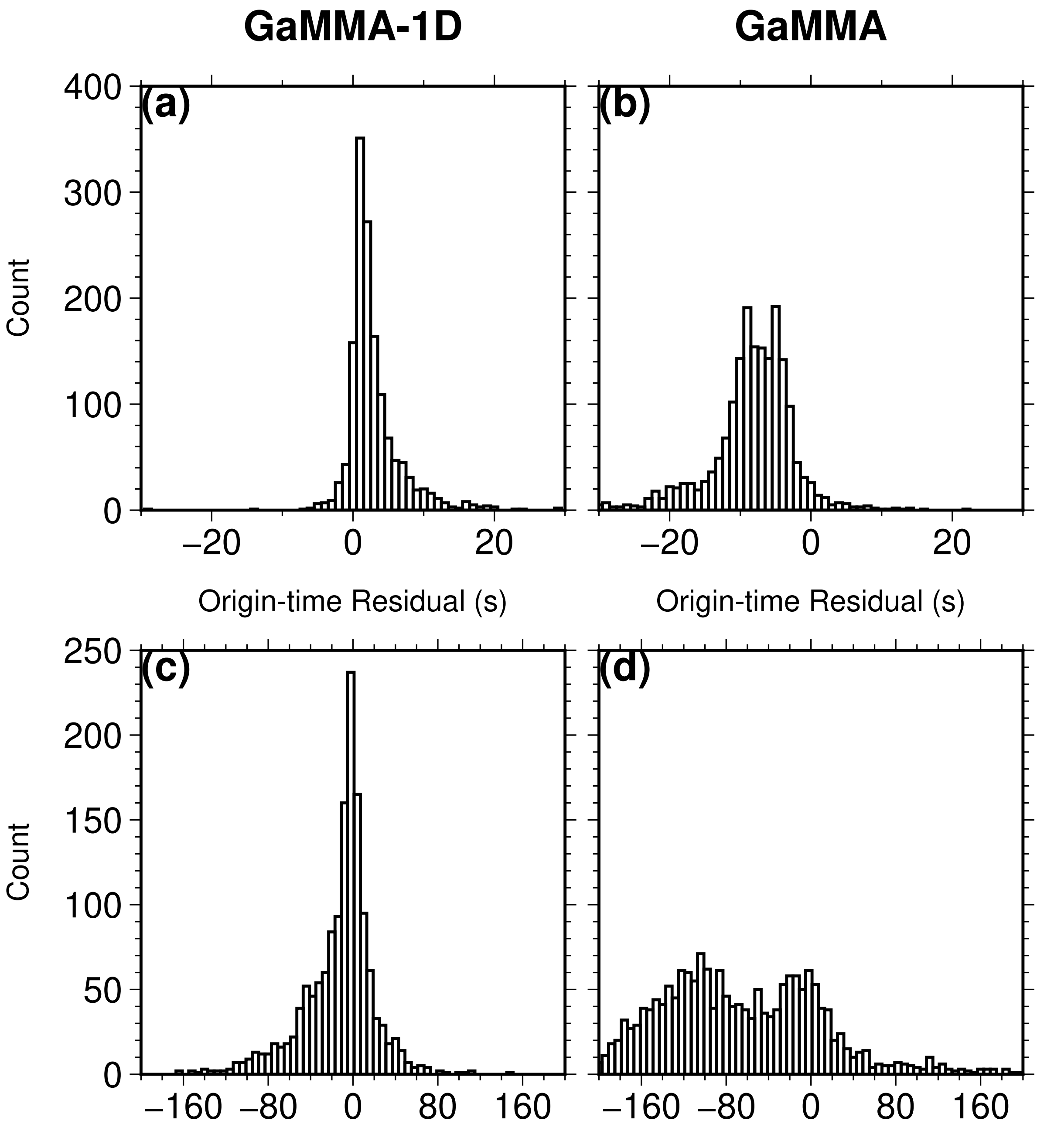

Figure 10. Origin-time (top) and depth (bottom) residuals for GaMMA-1D and GaMMA. When manual picks are associated by GaMMA-1D or GaMMA, the event origin times and depths are compared against the reference catalogue that was associated by the Antelope software (Wei et al. 2017).

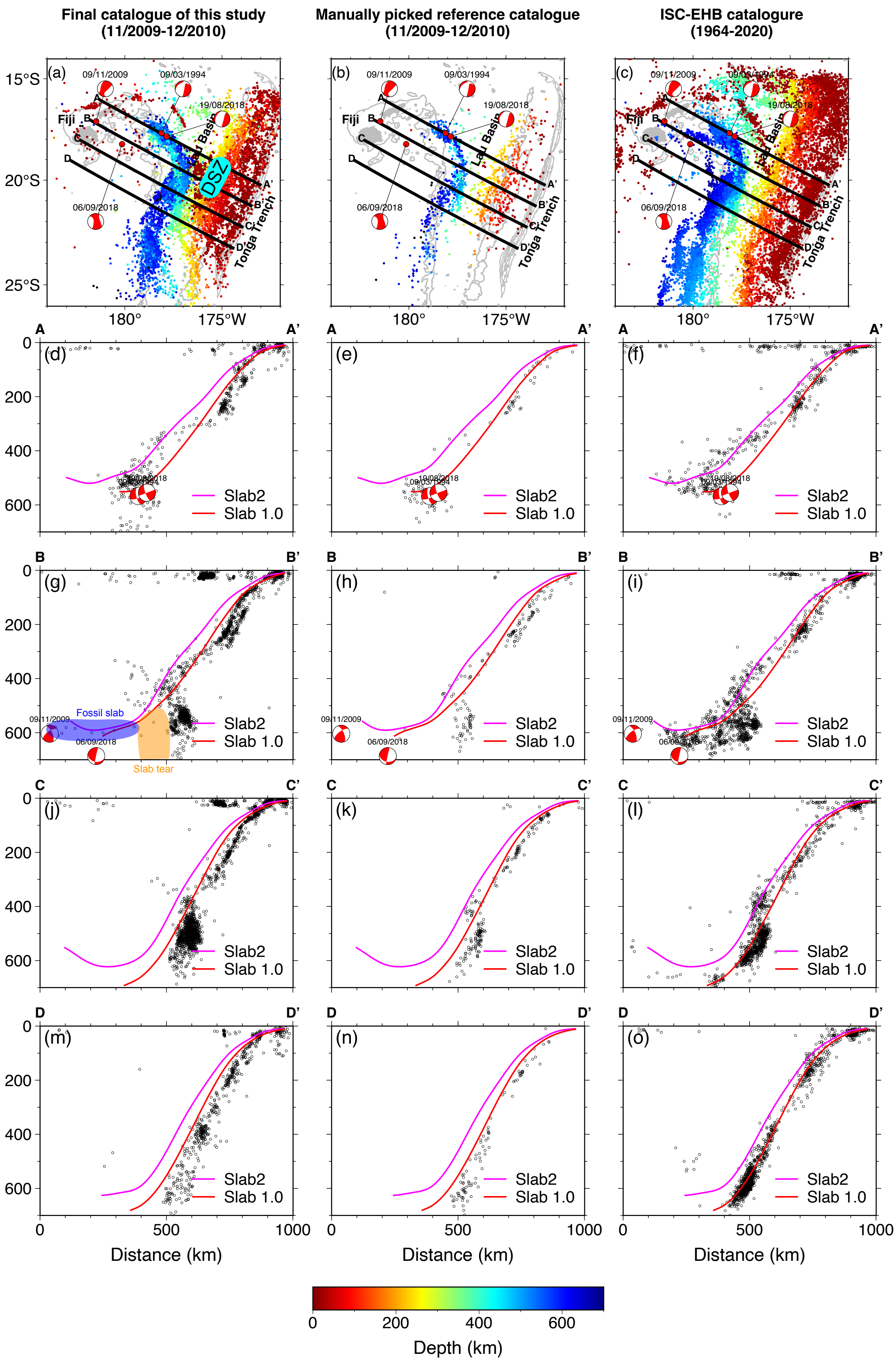
Final catalogue of this study
(11/2009-12/2010)
Manually picked reference catalogue
(11/2009-12/2010)
ISC-EHB catalogure
(1964-2020)
(a)
(b)
(c)
15°S
20°S
25°S
180°
175°W
09/11/2009
09/03/1994
19/08/2018
06/09/2018
Fiji
Lau Basin
DSZ
Tonga Trench
A
B
C
D
A'
B'
C'
D'
(d)
(e)
(f)
(g)
(h)
(i)
(j)
(k)
(l)
(m)
(n)
(o)
Slab2
Slab 1.0
Fossil slab
Slab tear
0
200
400
600
500
1000
Distance (km)
Depth (km)

Figure 11. Event distributions across 3 distinct catalogues. (Left column) Our final catalogue in this study. (Middle column) Reference catalogue by Wei et al. (2017). (Right column) ISC-EHB catalogue (International-Seismological-Centre 2023). In each column, the top panel shows the map view, similar to Figure 7, and the following panels show 4 cross-sections, similar to Figure 8. Beachballs show the focal mechanisms of 4 notable large deep earthquakes (1994/3/9 Mw 7.6, 2009/11/9 Mw 7.3, 2018/8/19 Mw 8.2, and 2018/9/6 Mw 7.9) from the Global CMT catalogue (Dziewonski et al. 1981; Ekström et al. 2012).

REFERENCES

Baer, M. & Kradolfer, U., 1987. An automatic phase picker for local and teleseismic events, *Bulletin of the Seismological Society of America*, **77**(4), 1437–1445.

Beyreuther, M., Barsch, R., Krischer, L., Megies, T., Behr, Y., & Wassermann, J., 2010. ObsPy: A Python Toolbox for Seismology, *Seismological Research Letters*, **81**(3), 530–533.

Bornstein, T., Lange, D., Münchmeyer, J., Woollam, J., Rietbrock, A., Barcheck, G., Grevemeyer, I., & Tilmann, F., 2023. PickBlue: Seismic phase picking for ocean bottom seismometers with deep learning, arXiv:2304.06635 [physics].

Brudzinski, M. R., Thurber, C. H., Hacker, B. R., & Engdahl, E. R., 2007. Global Prevalence of Double Benioff Zones, *Science*, **316**(5830), 1472–1474.

Cai, C. & Wiens, D. A., 2016. Dynamic triggering of deep earthquakes within a fossil slab, *Geophysical Research Letters*, **43**(18), 9492–9499.

Chai, C., Maceira, M., Santos-Villalobos, H. J., Venkatakrishnan, S. V., Schoenball, M., Zhu, W., Beroza, G. C., Thurber, C., & Team, E. C., 2020. Using a Deep Neural Network and Transfer Learning to Bridge Scales for Seismic Phase Picking, *Geophysical Research Letters*, **47**(16), e2020GL088651, _eprint: https://onlinelibrary.wiley.com/doi/pdf/10.1029/2020GL088651.

Chen, L.-C., Zhu, Y., Papandreou, G., Schroff, F., & Adam, H., 2018. Encoder-Decoder with Atrous Separable Convolution for Semantic Image Segmentation, arXiv:1802.02611 [cs].

Chen, M., Manea, V. C., Niu, F., Wei, S. S., & Kiser, E., 2019. Genesis of Intermediate-Depth and Deep Intraslab Earthquakes beneath Japan Constrained by Seismic Tomography, Seismicity, and Thermal Modeling, *Geophysical Research Letters*, **46**(4), 2025–2036, _eprint: https://onlinelibrary.wiley.com/doi/pdf/10.1029/2018GL080025.

Dziewonski, A. M., Chou, T., & Woodhouse, J. H., 1981. Determination of earthquake source parameters from waveform data for studies of global and regional seismicity, *Journal of Geophysical Research: Solid Earth*, **86**(B4), 2825–2852.

Ekström, G., Nettles, M., & Dziewoński, A. M., 2012. The global CMT project 2004–2010: Centroid-moment tensors for 13,017 earthquakes, *Physics of the Earth and Planetary Interiors*, **200**, 1–9, Publisher: Elsevier.

Engdahl, E. R., van der Hilst, R., & Buland, R., 1998. Global teleseismic earthquake relocation with improved travel times and procedures for depth determination, *Bulletin of the Seismological Society of America*, **88**(3), 722–743, Publisher: The Seismological Society of America.

Fan, W., Wei, S. S., Tian, D., McGuire, J. J., & Wiens, D. A., 2019. Complex and Diverse Rupture Processes of the 2018 $M\ w$ 8.2 and $M\ w$ 7.9 Tonga-Fiji Deep Earthquakes, *Geophysical Research Letters*, **46**(5), 2434–2448.

Florez, M. A. & Prieto, G. A., 2019. Controlling Factors of Seismicity and Geometry in Double Seismic Zones, *Geophysical Research Letters*, **46**(8), 4174–4181.

Gentili, S. & Michelini, A., 2006. Automatic picking of P and S phases using a neural tree, *Journal of Seismology*, **10**(1), 39–63.

Gong, J., Fan, W., & Parnell-Turner, R., 2023. Machine Learning-Based New Earthquake Catalog Illuminates On-Fault and Off-Fault Seismicity Patterns at the Discovery Transform Fault, East Pacific Rise, *Geochemistry, Geophysics, Geosystems*, **24**(9), e2023GC011043, _eprint: https://onlinelibrary.wiley.com/doi/pdf/10.1029/2023GC011043.

Green, H. W. & Houston, H., 1995. The Mechanics of Deep Earthquakes, *Annual Review of Earth and Planetary Sciences*, **23**(1), 169–213.

Hacker, B. R., Peacock, S. M., Abers, G. A., & Holloway, S. D., 2003. Subduction factory 2. Are intermediate-depth earthquakes in subducting slabs linked to metamorphic dehydration reactions?, *Journal of Geophysical Research: Solid Earth*, **108**(B1), 2001JB001129.

Hayes, G. P., Wald, D. J., & Johnson, R. L., 2012. Slab1.0: A three-dimensional model of global subduction zone geometries, *Journal of Geophysical Research: Solid Earth*, **117**(B1), _eprint: https://onlinelibrary.wiley.com/doi/pdf/10.1029/2011JB008524.

Hayes, G. P., Moore, G. L., Portner, D. E., Hearne, M., Flamme, H., Furtney, M., & Smoczyk, G. M., 2018. Slab2, a comprehensive subduction zone geometry model, *Science*, **362**(6410), 58–61, Publisher: American Association for the Advancement of Science.

Igarashi, T., Matsuzawa, T., Umino, N., & Hasegawa, A., 2001. Spatial distribution of focal mechanisms for interplate and intraplate earthquakes associated with the subducting Pacific plate beneath the northeastern Japan arc: A triple-planed deep seismic zone, *Journal of Geophysical Research: Solid Earth*, **106**(B2), 2177–2191.

International-Seismological-Centre, 2023. ISC-EHB dataset.

Jia, Z., Shen, Z., Zhan, Z., Li, C., Peng, Z., & Gurnis, M., 2020. The 2018 Fiji Mw 8.2 and 7.9 deep earthquakes: One doublet in two slabs, *Earth and Planetary Science Letters*, **531**, 115997, Publisher: Elsevier.

Kawakatsu, H., 1985. Double seismic zone in Tonga, *Nature*, **316**(6023), 53–55, Publisher: Nature Publishing Group UK London.

Kennett, B. L. N., Engdahl, E. R., & Buland, R., 1995. Constraints on seismic velocities in the Earth from traveltimes, *Geophysical Journal International*, **122**(1), 108–124.

Kita, S., Okada, T., Hasegawa, A., Nakajima, J., & Matsuzawa, T., 2010. Anomalous deepening of a seismic belt in the upper-plane of the double seismic zone in the Pacific slab beneath the Hokkaido corner: Possible evidence for thermal shielding caused by subducted forearc crust materials, *Earth and Planetary Science Letters*, **290**(3-4), 415–426, Publisher: Elsevier.

Liu, M., Zhang, M., Zhu, W., Ellsworth, W. L., & Li, H., 2020. Rapid Characterization of the July 2019 Ridgecrest, California, Earthquake Sequence From Raw Seismic Data Using Machine-Learning Phase Picker, *Geophysical Research Letters*, **47**(4), e2019GL086189, _eprint: https://onlinelibrary.wiley.com/doi/pdf/10.1029/2019GL086189.

Liu, M., Li, L., Zhang, M., Lei, X., Nedimović, M. R., Plourde, A. P., Guo, R., Wang, W., & Li, H., 2023. Complexity of initiation and evolution of the 2013 Yunlong earthquake swarm, *Earth and Planetary Science Letters*, **612**, 118168.

Loshchilov, I. & Hutter, F., 2019. Decoupled Weight Decay Regularization, arXiv:1711.05101 [cs, math].

Lu, C., Grand, S. P., Lai, H., & Garnero, E. J., 2019. TX2019slab: A New P and S Tomography Model Incorporating Subducting Slabs, *Journal of Geophysical Research: Solid Earth*, **124**(11), 11549–11567, _eprint: https://onlinelibrary.wiley.com/doi/pdf/10.1029/2019JB017448.

McBrearty, I. W. & Beroza, G. C., 2023. Earthquake phase association with graph neural networks, *Bulletin of the Seismological Society of America*, **113**(2), 524–547, Publisher: Seismological Society of America.

McGuire, J. J., Wiens, D. A., Shore, P. J., & Bevis, M. G., 1997. The March 9, 1994 (M_w 7.6), deep Tonga earthquake: Rupture outside the seismically active slab, *Journal of Geophysical Research: Solid Earth*, **102**(B7), 15163–15182.

Mousavi, S. M. & Beroza, G. C., 2022. Deep-learning seismology, *Science*, **377**(6607), eabm4470.

Mousavi, S. M. & Beroza, G. C., 2023. Machine Learning in Earthquake Seismology, *Annual Review of Earth and Planetary Sciences*, **51**(1), 105–129.

Mousavi, S. M., Sheng, Y., Zhu, W., & Beroza, G. C., 2019. STanford EArthquake Dataset (STEAD): A Global Data Set of Seismic Signals for AI, *IEEE Access*, **7**, 179464–179476, Conference Name: IEEE Access.

Mousavi, S. M., Ellsworth, W. L., Zhu, W., Chuang, L. Y., & Beroza, G. C., 2020. Earthquake transformer—an attentive deep-learning model for simultaneous earthquake detection and phase picking, *Nature Communications*, **11**(1), 3952, Number: 1 Publisher: Nature Publishing Group.

Park, Y., Mousavi, S. M., Zhu, W., Ellsworth, W. L., & Beroza, G. C., 2020. Machine-Learning-Based Analysis of the Guy-Greenbrier, Arkansas Earthquakes: A Tale of Two Sequences, *Geophysical Research Letters*, **47**(6), e2020GL087032, _eprint: https://onlinelibrary.wiley.com/doi/pdf/10.1029/2020GL087032.

Pesicek, J. D., Thurber, C. H., Zhang, H., DeShon, H. R., Engdahl, E. R., & Widiyantoro, S., 2010. Teleseismic double-difference relocation of earthquakes along the Sumatra-Andaman subduction zone using a 3-D model, *Journal of Geophysical Research*, **115**(B10), B10303.

Ronneberger, O., Fischer, P., & Brox, T., 2015. U-Net: Convolutional Networks for Biomedical Image Segmentation, in *Medical Image Computing and Computer-Assisted Intervention – MICCAI 2015*, Lecture Notes in Computer Science, pp. 234–241, Springer International Publishing, Cham.

Ross, Z. E., Meier, M., Hauksson, E., & Heaton, T. H., 2018. Generalized Seismic Phase Detection with Deep Learning, *Bulletin of the Seismological Society of America*, **108**(5A), 2894–2901.

Ross, Z. E., Cochran, E. S., Trugman, D. T., & Smith, J. D., 2020. 3D fault architecture controls the dynamism of earthquake swarms, *Science*, **368**(6497), 1357–1361, Publisher: American Association for the Advancement of Science.

Ruff, L. & Kanamori, H., 1980. Seismicity and the subduction process, *Physics of the Earth and Planetary Interiors*, **23**(3), 240–252.

Sleeman, R. & van Eck, T., 1999. Robust automatic P-phase picking: an on-line implementation in the analysis of broadband seismogram recordings, *Physics of the Earth and Planetary Interiors*, **113**(1), 265–275.

Tan, Y. J., Waldhauser, F., Ellsworth, W. L., Zhang, M., Zhu, W., Michele, M., Chiaraluce, L., Beroza, G. C., & Segou, M., 2021. Machine-Learning-Based High-Resolution Earthquake Catalog Reveals How Complex

Fault Structures Were Activated during the 2016–2017 Central Italy Sequence, *The Seismic Record*, **1**(1), 11–19.

Vaswani, A., Shazeer, N., Parmar, N., Uszkoreit, J., Jones, L., Gomez, A. N., Kaiser, , & Polosukhin, I., 2017. Attention is All you Need, in *Advances in Neural Information Processing Systems*, vol. 30, Curran Associates, Inc.

Webb, S. C. & Crawford, W. C., 1999. Long-period seafloor seismology and deformation under ocean waves, *Bulletin of the Seismological Society of America*, **89**(6), 1535–1542, Publisher: The Seismological Society of America.

Wei, S. S., Wiens, D. A., Zha, Y., Plank, T., Webb, S. C., Blackman, D. K., Dunn, R. A., & Conder, J. A., 2015. Seismic evidence of effects of water on melt transport in the Lau back-arc mantle, *Nature*, **518**(7539), 395–398, Publisher: Nature Publishing Group UK London.

Wei, S. S., Wiens, D. A., van Keken, P. E., & Cai, C., 2017. Slab temperature controls on the Tonga double seismic zone and slab mantle dehydration, *Science Advances*, **3**(1), e1601755, Publisher: American Association for the Advancement of Science.

Wei, S. S., Ruprecht, P., Gable, S. L., Huggins, E. G., Ruppert, N., Gao, L., & Zhang, H., 2021. Along-strike variations in intermediate-depth seismicity and arc magmatism along the Alaska Peninsula, *Earth and Planetary Science Letters*, **563**, 116878, Publisher: Elsevier.

Wiens, D. A., McGuire, J. J., & Shore, P. J., 1993. Evidence for transformational faulting from a deep double seismic zone in Tonga, *Nature*, **364**(6440), 790–793, Publisher: Nature Publishing Group UK London.

Wiens, D. A., McGuire, J. J., Shore, P. J., Bevis, M. G., Draunidalo, K., Prasad, G., & Helu, S. P., 1994. A deep earthquake aftershock sequence and implications for the rupture mechanism of deep earthquakes, *Nature*, **372**(6506), 540–543, Publisher: Nature Publishing Group UK London.

Wilding, J. D., Zhu, W., Ross, Z. E., & Jackson, J. M., 2023. The magmatic web beneath Hawai'i, *Science*, **379**(6631), 462–468, Publisher: American Association for the Advancement of Science.

Yamasaki, T. & Seno, T., 2003. Double seismic zone and dehydration embrittlement of the subducting slab, *Journal of Geophysical Research: Solid Earth*, **108**(B4), 2002JB001918.

Zhan, Z., 2020. Mechanisms and Implications of Deep Earthquakes, *Annual Review of Earth and Planetary Sciences*, **48**(1), 147–174.

Zhang, M., Ellsworth, W. L., & Beroza, G. C., 2019. Rapid Earthquake Association and Location, *Seismological Research Letters*, **90**(6), 2276–2284.

Zhu, W. & Beroza, G. C., 2019. PhaseNet: a deep-neural-network-based seismic arrival-time picking method, *Geophysical Journal International*, **216**(1), 261–273.

Zhu, W., McBrearty, I. W., Mousavi, S. M., Ellsworth, W. L., & Beroza, G. C., 2022. Earthquake Phase Association Using a Bayesian Gaussian Mixture Model, *Journal of Geophysical Research: Solid Earth*, **127**(5), e2021JB023249, _eprint: https://onlinelibrary.wiley.com/doi/pdf/10.1029/2021JB023249.

Zhu, W., Hou, A. B., Yang, R., Datta, A., Mousavi, S. M., Ellsworth, W. L., & Beroza, G. C., 2023. QuakeFlow: a scalable machine-learning-based earthquake monitoring workflow with cloud computing, *Geophysi-*

cal Journal International, **232**(1), 684–693.